Superfilamentation in air reconstructed by transversal interferometry

Aleksey Murzanev,[1] Sergey Bodrov [●],[2,1] Zhanna Samsonova,[3] Daniil Kartashov,[3] Michael Bakunov [●],[2] and Massimo Petrarca[4]

[1]*Institute of Applied Physics, Russian Academy of Sciences, 46 Ulyanov Street, Nizhny Novgorod 603950, Russia*
[2]*University of Nizhny Novgorod, 23 Gagarin Avenue, Nizhny Novgorod 603950, Russia*
[3]*Institute of Optics and Quantum Electronics, Abbe Center of Photonics, Friedrich-Schiller University Jena, Max-Wien-Platz 1, Jena 07743, Germany*
[4]*La Sapienza University, SBAI Department, via Antonio Scarpa 14, Rome 00161, Italy*

Multiple filamentation of terawatt femtosecond Ti:sapphire laser beams in air is experimentally investigated for intermediate external focusing conditions with the numerical apertures $NA = 10^{-2}$ and 4×10^{-3}. The electron density distribution in a multifilament plasma channel is measured by means of transversal interferometry. The results confirm the existence of superdense filaments (superfilaments). It is also found that the maximum electron density in filaments differs by an order of magnitude ($\sim 7 \times 10^{17}$ cm^{-3} and $\sim 9 \times 10^{16}$ cm^{-3}) for the two values of NA. This demonstrates high sensitivity of the multiple filamentation regime to focusing conditions. The interferometric results are compared with the spatially resolved measurements of the luminescence intensity from the multifilament plasma channel to verify the accuracy of the widely used luminescence technique.

I. INTRODUCTION

One of the main physical phenomena accompanying the propagation of high-peak-power femtosecond laser beams in air is filamentation [1] originating from the dynamic balance between diffraction, Kerr-induced self-focusing, and defocusing by the optically generated plasma [2,3]. The competition between these factors can result in a long-range propagation of high-intensity optical pulses and generation of long plasma channels (up to a distance of 1 km [4]) in air. The phenomenon of filamentation is accompanied by a wealth of physical effects, such as white-light generation [5–7], terahertz generation [8–10], and pulse self-compression [11], which can be useful for a variety of applications including remote sensing [6,12–14], terahertz spectroscopy [15], and generation of few-cycle ultrashort pulses [11]. The generation of plasma channels is also very attractive for lightning control [16], microwave [17,18] and optical [19] guiding, and standoff lasing in air [20].

Filamentation occurs if Kerr self-focusing prevails over diffraction divergence of the optical beam, which imposes condition $P > P_{cr}$ on the optical power P, with P_{cr} the critical power for self-focusing in air ($P_{cr} \sim 5$–10 GW at the optical wavelength of 800 nm [21]). For laser pulses with power up to $10P_{cr}$, a single plasma filament with plasma density in the range of 10^{16}–10^{17} cm^{-3} and a diameter of 100–150 μm is formed in the ambient air [3,22].

Further increasing the pump power, typically above $10P_{cr}$, leads to the development of modulational instability in the optical beam and gives rise to multiple filamentation [23,24]. In this regime, the number of filaments at first increases with the pump power (with a rate of one filament per $\sim 5P_{cr}$ [13,25]) and then saturates [26,27]. This demonstrates a significant role of the photon bath (or energy reservoir), i.e., the optical

beam portion surrounding filaments, in the filament formation [28,29].

The filamentation parameters can be controlled by laser beam ellipticity or astigmatism [30–32], initial chirp [13,24], external phase or amplitude masks [19,33,34], and external focusing [13,32,34–40]. In the single-filament regime, it was shown that tighter external focusing results in an increase of the plasma density and filament diameter [35]. The transition between the regimes of linear and nonlinear focusing governed by the geometric focusing and Kerr self-focusing, respectively, was investigated analytically and experimentally [41]. It was shown that for 800-nm laser pulses in air, the transition from a linear- to nonlinear-focusing regime typically falls in the interval of the numerical apertures $NA = 0.003$–0.005.

The propagation in air of femtosecond laser beams under the conditions of highly overcritical power and tight-focusing ($NA \sim 0.1$) was investigated in Refs. [36,37]. The experimental measurements and theoretical calculations demonstrated complete air ionization in the region about 1 mm long and 200–400 μm in transverse size with the plasma density about 3×10^{19} cm^{-3} or even higher. In the opposite case of loose focusing ($NA < 0.001$), multiple filamentation was observed in several works [6,13,38]. It was demonstrated that the position of the filamentation region and the filament length can be controlled by the degree of external focusing [38].

Multiple filamentation of laser beams in air at highly overcritical power and intermediate external focusing with $NA \sim 0.003$ (corresponding to the transition between linear and nonlinear focusing in the single-filament regime) was investigated in Ref. [40]. (Interestingly, for similar focusing conditions a single-filament regime was observed in condensed matter [42].) Measurements of the plasma luminescence showed that in the focus region there exists a bundle of

closely packed filaments with the plasma density in a filament an order of magnitude higher than in the standard filament in the prefocus region. The superdense filaments were dubbed superfilaments [40]. The luminescence technique only provided a comparative assessment of the two types of filaments; absolute measurements of the plasma density in the filaments were not done.

Quantitative experimental characterization of the electron density distribution in laser-created plasma channels is of high importance both for the physical understanding of the nonlinear laser propagation, in particular, identifying the filamentation regimes, and for the application purposes, such as optimization of the filament parameters for using it as a terahertz emitter or a microwave waveguide. Particularly, high-density filaments (such as superfilaments) are a promising gain medium for the generation of a strong lasing effect from femtosecond filaments. Various approaches have been used for characterization of the filament plasmas. The most widely used techniques include measuring plasma electrical conductivity [43–45], nitrogen fluorescence [35,40], and acoustic emission from plasma [46], as well as transverse [47] and longitudinal [35] diffractometry of a probe laser beam, and interferometric [22,48–50] and holographic methods [51]. The methods based on measuring the plasma conductivity or emissions from plasma involve spatiotemporal averaging and are problematic to calibrate. The most detailed and accurate information about filament structure can be obtained by interferometric methods.

For typical plasma densities ($\sim 10^{16}$–10^{17} cm^{-3}) and diameters (~ 100–200 μm) of filaments in air, the phase shifts in the transverse optical interferometry are extremely small (~ 0.01 rad) [22]. Measuring such small shifts requires special processing of interferometric images [22]. Despite the complexity of the interferometric approach, it has an advantage of providing direct and accurate information on the filament structure. In the single-filament regime, time-resolved interferometric measurements of the transverse distribution of the electron density with a maximum value of $\sim 10^{17}$ cm^{-3} were performed in Ref. [22].

In this paper, we implement such measurements in the more complex regime of multiple filamentation. In particular, we measured the transverse electron density profile in the plasma channel created in air by a high-power ($\sim 300 P_{\rm cr}$) femtosecond laser pulse for two external focusing conditions with NA $= 10^{-2}$ and 4×10^{-3}. This allowed us to verify the regime of superfilamentation, introduced in Ref. [40], by direct interferometric measurements. In particular, we show that superfilament formation is rather sensitive to the focusing conditions. The plasma density in filaments drops by an order of magnitude, i.e., from $\sim 7 \times 10^{17}$ cm^{-3} to $\sim 9 \times 10^{16}$ cm^{-3}, with a decrease of NA from 10^{-2} to 4×10^{-3}.

We compare our interferometric results with the spatially resolved measurements of the luminescence intensity from the multifilament plasma channel to verify the accuracy of the widely used luminescence technique.

II. EXPERIMENTAL SETUP

A multiterawatt Ti:sapphire laser system JETI-40 with 30-fs pulse duration and a wavelength of $\lambda = 800$ nm was
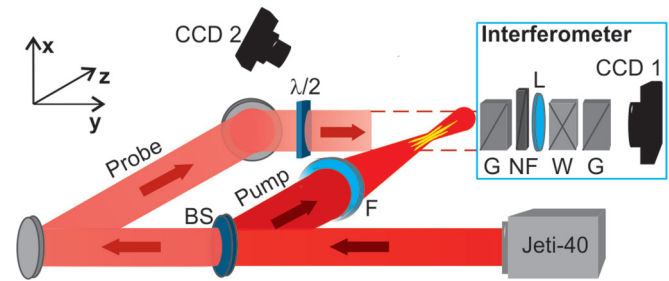

FIG. 1. Experimental setup.

used for the investigation of multiple filamentation in the ambient air under intermediate focusing conditions. A pump beam with linear polarization and a diameter of about 6 cm [full width at half maximum (FWHM) of a super-Gaussian shape] was focused by a lens with the focal length $f = 300$ or 750 cm (corresponding NA is 10^{-2} and 4×10^{-3}) in air (Fig. 1). The filamentation dynamics of super-Gaussian beams at very high powers can differ from that of Gaussian beams [52]. In our experiment, however, the intensity distribution in the geometric focus was optimized at a low (smaller than $P_{\rm cr}$) power by using a deformable mirror. The beam propagating in a vacuum beamline (with a residual pressure of 10^{-4} mbar) was coupled to the ambient air through a 2-cm-thick antireflective (AR)-coated BK7 optical window. In the case of shorter focusing ($f = 300$ cm), the focusing lens was placed outside of the vacuum chamber at a distance of about 30 cm from the vacuum window. In the case of longer focusing ($f = 750$ cm), the focusing lens was placed in the vacuum beamline and the beam path about 2 m in length was folded by several mirrors in vacuum. The maximum energy of the pump beam (measured after the window) was 130 mJ, which corresponds to the peak power of 3.2 TW or $\sim 320 P_{\rm cr}$ (calculated by taking into account stretching of the pulse up to ~ 40 fs in the vacuum window and assuming $P_{\rm cr} = 10$ GW).

To investigate the spatial distribution of the plasma density at different positions along the laser beam (z axis, Fig. 1), we used the interferometric and luminescence techniques. In the first technique, a weak collimated probe laser beam passed a delay line, traversed (along the y axis) the filamentation region orthogonally, and was detected by a Nomarski interferometer [53]. The interferometer (Fig. 1) consisted of an imaging lens (L), charge-coupled device (CCD) camera (CCD1), Wollaston prism (W), and two Glan-Taylor prisms (G1 and G2). The Wollaston prism (W) split the probe optical beam into two parts with orthogonal polarizations. After passing the analyzer G2 oriented at $45°$ to the polarizer G1 these two beams formed interference fringes in the overlap region, which were recorded by the CCD1 camera. A part of the probe beam propagating through the plasma in filaments with electron density $n_e(x, y, z)$ experienced phase retardation

$$\Delta \varphi(x, z) = \frac{\pi}{\lambda N_{e0}^{cr}} \int n_e(x, y, z) dy, \qquad (1)$$

where $N_{e0}^{cr} = 1.1 \times 10^{21} / \lambda \, [\mu\text{m}]^2 = 1.7 \times 10^{21}$ cm^{-3} is the critical plasma density. This retardation led to a shift of fringes in the interferometric pattern. The lens L relay imaged the plasma filaments to the CCD1 camera with a

0.5 demagnification and $\sim$20-μm spatial resolution. To enlarge the region of the interference limited by the probe pulse duration, a 10-nm-bandwidth notch filter (NF) was placed in front of the lens L. To minimize the background illumination of the CCD1 camera by the scattered pump radiation, the polarization of the probe beam before the CCD1 camera was set orthogonal to the polarization in the pump beam by a $\lambda/2$ wave plate placed before the filament. The delay line in the probe beam path (not shown in Fig. 1) was adjusted to probe the plasma density distribution with a delay of $\sim$10 ps after the pump pulse. This time is significantly less than the electron recombination time in air plasma, which is about hundreds of picoseconds [22,54].

The interferometric part of the experimental setup was installed on a motorized translation stage with the translation range of 40 cm along the pump beam. This range covered the regions before and after the geometric focus and was scanned by shifting the interferometer with 2-cm steps. For each position, 100 single-shot interferometric images of filaments and 100 background interferometric images with blocked pump beam were recorded. By applying the two-dimensional (2D) fast Fourier transform (FFT) technique [55], phase maps from both signal and background interferometric images were obtained [22]. To retrieve spatial phase distribution with minimum noise, each of the 100 background phase maps was subtracted from each signal phase map. For each signal phase map, differential phase maps with minimum noise level were selected and averaged to obtain the best signal-to-noise ratio single-shot differential phase maps containing information about the plasma density in the filaments. Too noisy signal maps were discarded. As a result, from 100 signal phase maps for each position we typically obtained from several to several tens (depending on the magnitude of the signal) good quality single-shot phase maps. Owing to laser energy and pump beam pointing fluctuations, as well as to the statistical nature of multifilamentation, fine details in the phase maps were not reproducible from shot to shot. However, a general large-scale structure of the plasma channel, such as splitting into multiple plasma strings, was preserved. In what follows, if not otherwise specified, we show the most frequent single-shot phase distributions measured in the experiments. Note that, because of low plasma density for $f = 750$ cm, an additional digital filter was applied to the phase maps to reduce the noise.

To measure luminescence from the multifilament plasma channel, we used one more CCD camera (CCD2 in Fig. 1) triggered simultaneously with CCD1. The luminescence camera was placed at a small ($\sim$15°) angle to the probe beam in the vertical plane perpendicular to the pump beam. The resolution of the luminescence images was about 15 μm.

III. RESULTS

The phase maps and corresponding luminescence images at different scan positions z_s along the laser beam for the case $f = 300$ cm are shown in Fig. 2 ($z_s = 0$ corresponds to the geometric focus). In the region before the geometric focus (negative values of z_s in Fig. 2), several plasma strings are well distinguished in both the phase maps [Fig. 2(a)] and luminescence images [Fig. 2(b)]. An example of statistical shot-to-shot variations of the phase maps is shown in Fig. 3
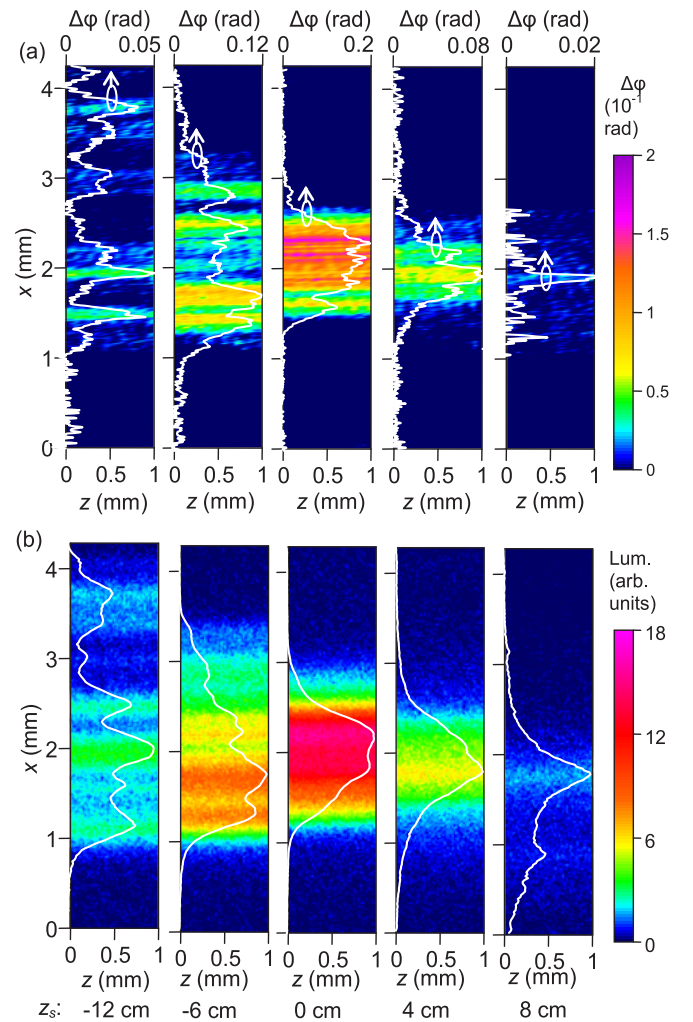

FIG. 2. (a) 2D phase maps at different positions z_s (shown at the bottom) for $f = 300$ cm. White curves show the transverse profiles of the phase retardation averaged along the z axis (the scales are shown at the top of the 2D images). (b) Images of the plasma luminescence for the corresponding positions z_s.

for the position $z_s = -12$ cm before the geometric focus. For the snapshot in Figs. 3(a) and 3(b), about seven filaments of $\sim$130 μm diameter (FWHM) with the maximum phase retardation $\Delta\varphi_m = 0.03$–0.05 rad are well discernible in the central part ($1 < x < 2.8$ mm) of the plasma channel. For the snapshot in Figs. 3(c) and 3(d), the plasma strings in the central part become closer to each other and partially overlap, resulting in three filaments with a diameter of $\sim$300 μm and an $\sim$20% higher peak value of the phase retardation. Formation of these relatively thick plasma structures can be attributed to partial overlapping of the filament projections onto the cross section of the probe beam. The total amount of filaments M_f, both in the central and peripheral regions of the plasma channel at $z_s = -12$ cm, varies in the 9–15 range from shot to shot.

A comparison of the phase maps [Fig. 2(a)] and luminescence images [Fig. 2(b)] at $z_s = -12$ cm demonstrates a good correlation between the two techniques. At the same time, the luminescence images look somewhat smoother,
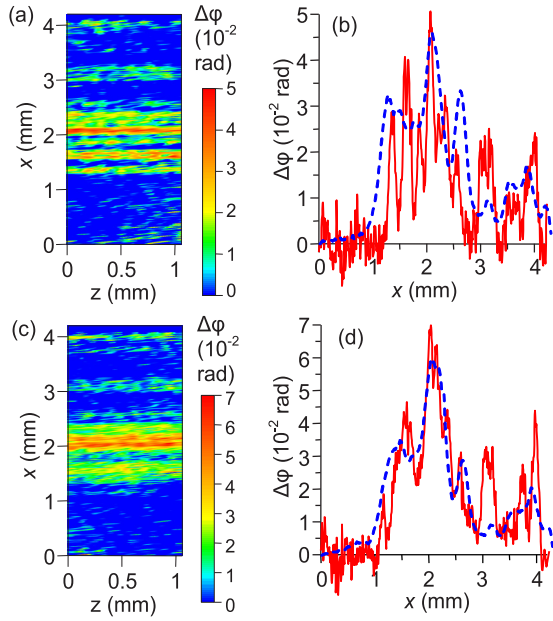
FIG. 3. (a),(c) 2D phase maps and corresponding (b),(d) transverse profiles of the phase retardation $\Delta\varphi$ at $z_s = -12$ cm for two different snapshots, $f = 300$ cm. Dashed lines in (b),(d) trace the corresponding transverse profiles of luminescence.

which is also confirmed by a comparison of the transverse profiles in Figs. 3(b) and 3(d). In the case of separated filaments [Fig. 3(b)], the luminescence technique does not resolve this fine multifilament structure. In the case of filament overlapping and formation of a larger-scale plasma structure [Fig. 3(d)], the interferometric and luminescence techniques agree well. The difference between the profiles at the periphery ($3 < x < 4$ mm) of the plasma channel in Figs. 3(b) and 3(d) can be explained by the out-of-plane position of the luminescence imaging camera CCD2.

To estimate the plasma density in individual filaments, we assumed a Gaussian transverse profile of the electron density in the filaments and matched the theoretically calculated $\Delta\varphi(x)$ with the measured profiles. Using a super-Gaussian profile, which is more appropriate for filaments [22], did not substantially alter the plasma density values retrieved with the Gaussian fit. The calculations result in the maximum plasma density $N_e = (1–2) \times 10^{17}$ cm^{-3} for the central part of the multifilament plasma channel and $N_e = (0.7–1.5) \times 10^{17}$ cm^{-3} for the peripheral region. The plasma density intervals that are pointed out account for both the shot-to-shot deviations and filament-to-filament variations for the same single shot. The FWHM diameter of a filament is in the 100–140 μm range. The obtained plasma densities agree well with the critical electron concentration N_e^{cr} for oblique incidence of laser radiation on the plasma boundary with a grazing angle θ defined by the beam convergence after the focusing lens:

$$N_e^{cr} = N_{e0}^{cr}\sin^2(\theta) \approx N_{e0}^{cr}(\text{NA})^2. \qquad (2)$$

For NA $= 0.01$, Eq. (2) gives $N_e^{cr} = 1.7 \times 10^{17}$ cm^{-3} which is close to the upper level of the plasma density estimated from the experiment. It should be noted that the depth of field in the
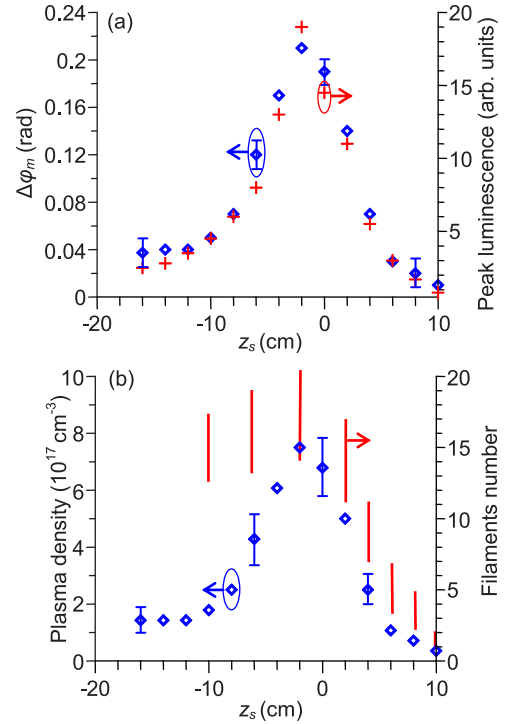

FIG. 4. (a) Maximum phase retardation $\Delta\varphi_m$ (blue diamonds) and peak luminescence (red crosses) as functions of the coordinate along the plasma channel z_s. (b) Plasma density N_e estimated from $\Delta\varphi_m$ (blue diamonds and circles) and range of total filament number M_f (red segments) as functions of z_s. The error bars at some diamonds show the typical statistical dispersion of $\Delta\varphi_m$ and plasma density for different z_s. The focal length is $f = 300$ cm.

phase shift measurements was $\sim$1 mm, which is smaller than the diameter of the plasma channel in the prefocus region. Due to this fact some of the filaments could be out of the object plane of the imaging system. This would result in a smoothing of the phase profile not substantially affecting the estimated values of the plasma density in the filaments.

By approaching the geometric focus ($z_s = -6$ cm in Fig. 2), the plasma strings become packed denser and the phase retardation in each of them rapidly increases (see also Fig. 4). From shot to shot, smooth or crownlike transverse profiles of the phase retardation were measured within an individual string. By analyzing several profiles with visually separated filaments, we did not observe substantial changes in the filament diameter. With use of a known diameter we estimate the plasma density in a filament in the central region of the plasma channel as $N_e = (3–5) \times 10^{17}$ cm^{-3}. The total number of filaments is in the 13–18 range and does not vary substantially from shot to shot.

In the geometric focus ($z_s = 0$ cm in Fig. 2), the plasma strings seem to be merging and producing a super-Gaussian-like transverse profile of the phase retardation with evident modulation at the top. If we assume that this profile corresponds to a single smooth plasma channel (with FWHM transverse size of about 1.5 mm), the maximum plasma density can be estimated as about 10^{17} cm^{-3}. This value is not consistent with several times higher plasma densities in the filaments before the focus as estimated above. Therefore,

this counterintuitive drop in the plasma density suggests that the filaments do not merge inside the 1.5-mm-wide plasma channel but remain isolated. This conclusion is supported by a modulation at the top of the phase distribution in Fig. 2(a), which can be associated with the individual filaments and gives approximately the same filament number (14–20) as in the prefocus region. By taking the same filament diameter as in the prefocus region, the plasma density in each filament can be estimated as about $(6–8) \times 10^{17}$ cm^{-3}. It is worth noting that the corresponding luminescence image [Fig. 2(b)] has a smoother transverse profile than the phase map thus leading to an erroneous conclusion about a uniform millimeter-wide plasma channel.

In the region behind the geometric focus [$z_s = 4$ and 8 cm in Fig. 2(a)], the maximum value and width of the phase retardation distribution decrease monotonically. This can be attributed to a decrease both in the plasma density in each filament and in the number of filaments. For $z_s = 4$ cm, the distribution has a large-scale modulated Gaussian profile and contains about 7–11 filaments with the plasma density of $\sim 2 \times 10^{17}$ cm^{-3}. For $z = 8$ cm, we observed one or two filaments with the plasma density of $\sim 1 \times 10^{17}$ cm^{-3} and the diameter of ~ 100 μm.

Figure 4 summarizes the above given consideration on the evolution of the filament parameters along the laser path. In Fig. 4(a), the curves for the phase retardation $\Delta\varphi_m(z_s)$ and peak luminescence practically coincide, thus demonstrating a good correlation of the corresponding techniques. In Fig. 4(b), the plasma density $N_e(z_s)$ was estimated from $\Delta\varphi_m(z_s)$ by assuming a Gaussian profile of the electron concentration with a constant diameter of 120 μm. For $-16 < z_s < -10$ cm, the plasma density is about 1.5×10^{17} cm^{-3} and does not change significantly along the laser path (the region $z_s < -16$ cm was not investigated). When approaching the focus, N_e starts to grow, reaches a maximum of $\sim 7 \times 10^{17}$ cm^{-3} near $z_s = 0$, and then drops rapidly below $\sim 10^{17}$ cm^{-3} at $z_s = 10$ cm. Such behavior of the plasma density confirms the existence of the superfilamentation regime introduced in Ref. [40]. The superfilamentation regime occurs in the region $-10 < z_s < 4$ cm, where filaments converge to a dense bundle still remaining separated and of the same diameter.

The number of filaments M_f given in Fig. 4(b) was estimated from the transverse size of the plasma channel and modulation scale in the transverse distribution of the plasma density. In the prefocus and focus regions ($-16 < z_s < 0$ cm), M_f does not change substantially along the laser path and lies in the range between 12 and 20. Behind the geometric focus, M_f decreases rapidly so that only one or two filaments are observed at $z_s = 10$ cm.

For a longer focus lens ($f = 750$ cm), the evolution of the multifilament structure along the laser path is substantially different (Fig. 5). In the prefocus region ($z_s = -22$ cm), several strings of $\Delta\varphi$ are seen. Similar to the case $f = 300$ cm, these strings can correspond to single filaments or several partially overlapped filaments. The total number of filaments can be estimated as from 5 to 8. The characteristic transverse size (FWHM) of each filament varies insignificantly and lies in the 120–180 μm range that is a little larger than in the case of a shorter focus lens (120 μm). The maximum plasma density in each filament can be estimated as about
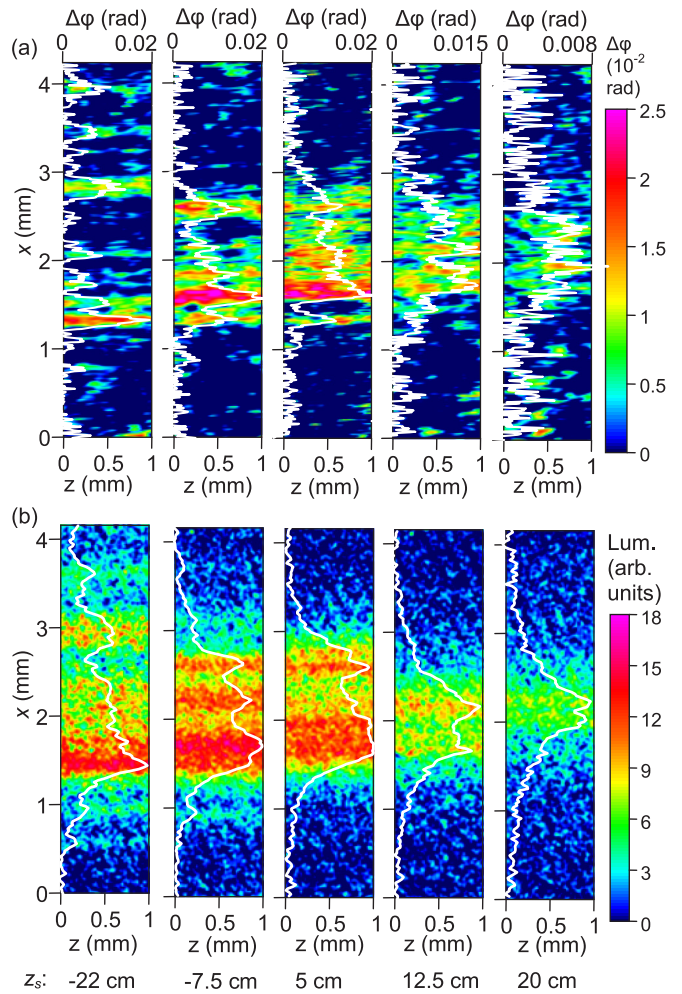

FIG. 5. (a) 2D phase maps for $f = 750$ cm at different positions z_s (shown at the bottom). White curves show the transverse profiles of the phase retardation averaged along the z axis (the scales are shown at the top of the 2D images). (b) Images of the plasma luminescence for the corresponding positions z_s.

$(4–6) \times 10^{16}$ cm^{-3}. This value is ~ 4 times smaller than for $f = 300$ cm and is in good agreement with the estimation on the basis of Eq. (2). The transverse profile of the luminescence intensity agrees qualitatively with the phase retardation profile although it shows a smoother behavior.

In the vicinity of the geometric focus ($z_s = -7.5$ and 5 cm), the plasma strings approach each other but remain isolated. This conclusion can be supported by three statistical snapshots with different transverse profiles for $z_s = -2.5$ cm (Fig. 6). In Figs. 6(a) and 6(c), several similar filaments are clearly seen [$M_f = 5$ in Fig. 6(a) and $M_f = 5–7$ in Fig. 6(c)], whereas in Fig. 6(b) the distribution has a prominent peak. The presence of the peak can be attributed to a higher plasma density in a single filament or probe beam passing through a few overlapped filaments. The difference in the distributions in Figs. 6(a)–6(c) can be explained by the stochastic nature of the multifilamentation process and by laser energy fluctuations.

For direct comparison of the luminescence and interferometric techniques, the luminescence profiles are also depicted by a dashed blue line in Figs. 6(a)–6(c). In Fig. 6(a), the
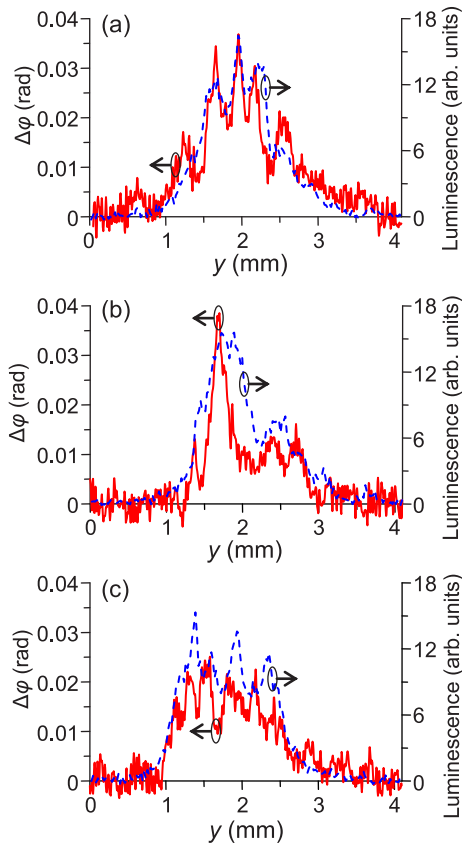
FIG. 6. Transverse profiles of the phase retardation (solid line) and luminescence (dashed line) at $z_s = -2.5$ cm for different snapshots; $f = 750$ cm.

FIG. 7. (a) Maximum phase retardation $\Delta\varphi_m$ (blue diamonds) and peak luminescence (red crosses) as functions of the position z_s. (b) Plasma density estimated from $\Delta\varphi_m$ (blue diamonds and circles) and range of total filaments number M_f (red segments) as functions of z_s. The error bars at some diamonds show typical statistical dispersion of $\Delta\varphi_m$ and plasma density for different z_s. The focal length is $f = 750$ cm.

luminescence and phase retardation curves practically coincide, but in Fig. 6(b) the peak of luminescence is about 2 times wider than the phase peak. Such a difference can be explained and even can serve as evidence of a particular alignment of two (or more) filaments along the direction of view. Indeed, two filaments, which are strictly aligned along the path of the probe laser pulse, will give a spike of the phase retardation with a size corresponding to one filament. At the same time, due to a slightly different angle of view in the luminescence setup, these two filaments will give a wider size of the corresponding peak in the luminescence image. If we assumed that the spike corresponds to one filament with a higher plasma density, the two measurement techniques would give identical spike widths. Thus, different angles of view in the luminescence and interferometric techniques should be used for a comparison of the fine structures of the luminance and phase curves.

Estimations of the plasma density in the filaments show that for $f = 750$ cm the plasma density varies with z_s in the region -25 cm $< z_s < 0$ not so strongly as for $f = 300$ cm: only from $\sim 5 \times 10^{16}$ cm^{-3} at $z_s = -25$ cm to $\sim 9 \times 10^{16}$ cm^{-3} at $z_s = 0$ [Fig. 7(b)]. Interestingly, despite the several times smaller number of filaments in the focus region for $f = 750$ cm than for $f = 300$ cm [cf. Figs. 4(b) and 7(b)] the transverse size of the focal plasma channel (the filament bundle) is approximately the same (1–1.5 mm) for both
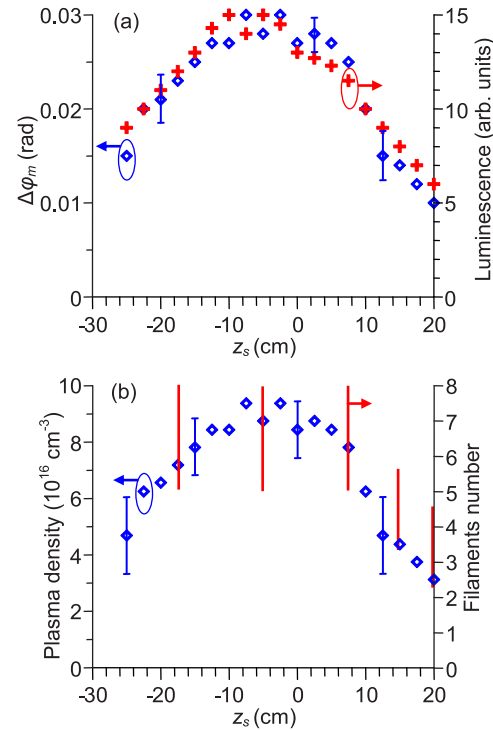
focusing conditions. This can be explained by denser packing of filaments and their smaller diameter for $f = 300$ cm.

Moving further past the focus ($z_s = 12$ and 20 cm in Figs. 5 and 7), the filaments converge closer, producing a crownlike distribution. If we assume that these filaments form a single plasma channel with a transverse size (FWHM) of about 1.4 mm (for $z_s = 12$ cm), the maximum plasma density in this channel can be estimated as $\sim 8 \times 10^{15}$ cm^{-3}. This density is significantly smaller than the density in the filaments before the focus. In addition, the modulation visible in the interferometric images suggests an occurrence of several closely packed filaments. From the analysis of several snapshots, we conclude that the number of filaments tends to decrease after the focus [Fig. 7(b)]. By assuming that the plasma channel consists of partially overlapping filaments with a transverse size of 140 μm, the maximum density in a filament can be estimated as $\sim 4.5 \times 10^{16}$ cm^{-3} for $z_s = 12$ cm and $\sim 3 \times 10^{16}$ for $z_s = 20$ cm.

As was mentioned above, the plasma diagnostics by the interferometric and luminescence techniques showed good correlation. Let us discuss the specifics of these techniques in more detail. In both techniques, the measured signals (phase retardation and luminescence intensity) are proportional to the plasma density (see Eq. (1) and Ref. [35], respectively). However, these two diagnostic methods have a significantly different temporal resolution. In the interferometric setup the captured phase retardation distribution is averaged over

the traveling time of the probe pulse through the filament, which is about several picoseconds. This time is much shorter than the characteristic filament lifetime, which is ~ 100 ps [22,54]. Thus, the interferometric technique gives a practically instantaneous plasma density distribution. In the luminescence technique, the plasma luminescence originates mainly from the second positive band of electronic transitions in N_2 molecules having a lifetime comparable to or longer than the electron recombination time. This leads to averaging over the temporal evolution of the plasma and smoothing the structure in luminescence images.

IV. CONCLUSION

The results of our interferometric measurements of the electron density distributions in the plasma channels created in air by high-power ($\sim 300 P_{cr}$) femtosecond laser pulses under the moderate ($NA = 10^{-2}$ and 4×10^{-3}) focusing conditions confirm the existence of the superfilamentation regime, introduced in Ref. [40]. We observed that the plasma channel consists of a bundle of highly dense filaments (or plasma strings), which converge, but do not merge, in the focal region.

The diameters of the plasma channel (~ 1–1.5 mm in the focal region) and plasma strings (~ 100–180 μm, not changing substantially along the laser beam) were almost the same for both values of NA. At the same time, we found that

other filamentation parameters, such as the number of plasma strings and plasma density in a string, depend substantially on the focusing conditions. In particular, the number of plasma strings is in the 10–20 range for $NA = 10^{-2}$ and only 5–8 for $NA = 4 \times 10^{-3}$. For $NA = 10^{-2}$, the plasma density increases from $N_e = (1$–$2) \times 10^{17}$ cm^{-3} in the prefocal region up to $(6$–$8) \times 10^{17}$ cm^{-3} in the focal region, whereas for $NA = 4 \times 10^{-3}$, the increase is much less pronounced: from $N_e = (4$–$6) \times 10^{16}$ to $\sim 9 \times 10^{16}$ cm^{-3}. This allows us to conclude that the multiple filamentation regime is very sensitive to the external focusing conditions.

By comparing the interferometric and luminescence measurements, we confirmed the applicability of the luminescence technique to investigating the structure of multifilament plasma channels. At the same time, this technique does not allow one to measure absolute values of the plasma density and provides a lower spatial resolution as compared to the interferometric method.

[1] A. Braun, G. Korn, X. Liu, D. Du, J. Squier, and G. Mourou, Opt. Lett. **20**, 73 (1995).

[2] S. L. Chin, S. A. Hosseini, W. Liu, Q. Luo, F. Théberge, N. Aközbek, A. Becker, V. P. Kandidov, O. G. Kosareva, and H. Schroeder, Can. J. Phys. **83**, 863 (2005).

[3] A. Couairon and A. Mysyrowicz, Phys. Rep. **441**, 47 (2007).

[4] M. Durand, A. Houard, B. Prade, A. Mysyrowicz, A. Durécu, B. Moreau, D. Fleury, O. Vasseur, H. Borchert, K. Diener, R. Schmitt, F. Théberge, M. Chateauneuf, J.-F. Daigle, and J. Dubois, Opt. Express **21**, 26836 (2013).

[5] H. Nishioka and K.-I. Ueda, Appl. Phys. B **77**, 171 (2003).

[6] M. Rodriguez, R. Bourayou, G. Méjean, J. Kasparian, J. Yu, E. Salmon, A. Scholz, B. Stecklum, J. Eislöffel, U. Laux, A. P. Hatzes, R. Sauerbrey, L. Wöste, and J.-P. Wolf, Phys. Rev. E **69**, 036607 (2004).

[7] Y. Petit, S. Henin, W. M. Nakaema, P. Béjot, A. Jochmann, S. D. Kraft, S. Bock, U. Schramm, K. Stelmaszczyk, P. Rohwetter, J. Kasparian, R. Sauerbrey, L. Wöste, and J.-P. Wolf, Phys. Rev. A **83**, 013805 (2011).

[8] C. D. Amico, A. Houard, S. Akturk, Y. Liu, J. Le Bloas, M. Franco, B. Prade, A. Couairon, V. T. Tikhonchuk, and A. Mysyrowicz, New J. Phys. **10**, 013015 (2008).

[9] T.-J. Wang, J.-F. Daigle, Y. Chen, C. Marceau, F. Théberge, M. Châteauneuf, J. Dubois, and S. L. Chin, Laser Phys. Lett. **7**, 517 (2010).

[10] J.-F. Daigle, F. Théberge, M. Henriksson, T.-J. Wang, S. Yuan, M. Châteauneuf, J. Dubois, M. Piché, and S. L. Chin, Opt. Express **20**, 6825 (2012).

[11] A. Mysyrowicz, A. Couairon, and U. Keller, New J. Phys. **10**, 025023 (2008).

[12] J. Kasparian, M. Rodriguez, G. Méjean, J. Yu, E. Salmon, H. Wille, R. Bourayou, S. Frey, Y. B. Andre, A. Mysyrowicz, R. Sauerbrey, J. P. Wolf, and L. Wöste, Science **301**, 61 (2003).

[13] P. Béjot, L. Bonacina, J. Extermann, M. Moret, J. P. Wolf, R. Ackermann, N. Lascoux, R. Salamé, E. Salmon, J. Kasparian, L. Bergé, S. Champeaux, C. Guet, N. Blanchot, O. Bonville, A. Boscheron, P. Canal, M. Castaldi, O. Hartmann, C. Lepage *et al.*, Appl. Phys. Lett. **90**, 151106 (2007).

[14] M. Petrarca, S. Henin, N. Berti, M. Matthews, J. Chagas, J. Kasparian, J.-P. Wolf, G. Gatti, G. Di Pirro, M.-P. Anania, M. Ferrario, and A. Ghigo, Appl. Phys. B **114**, 319 (2014).

[15] B. Clough, J. Dai, and X.-C. Zhang, Mater. Today **15**, 50 (2012).

[16] S. B. Leonov, A. A. Firsov, M. A. Shurupov, J. B. Michael, M. N. Shneider, R. B. Miles, and N. A. Popov, Phys. Plasmas **19**, 123502 (2012).

[17] M. Châteauneuf, S. Payeur, J. Dubois, and J.-C. Kieffer, Appl. Phys. Lett. **92**, 091104 (2008).

[18] B. Prade, A. Houard, J. Larour, M. Pellet, and A. Mysyrowicz, Appl. Phys. B **123**, 40 (2017).

[19] N. Jhajj, E. W. Rosenthal, R. Birnbaum, J. K. Wahlstrand, and H. M. Milchberg, Phys. Rev. X **4**, 011027 (2014).

[20] *Air Lasing*, edited by P. Polynkin and Y. Cheng, Springer Series in Optical Sciences (Springer International Publishing, Berlin, 2018).

[21] W. Liu and S. L. Chin, Opt. Express **13**, 5750 (2005).

[22] S. Bodrov, V. Bukin, M. Tsarev, A. Murzanev, S. Garnov, N. Aleksandrov, and A. Stepanov, Opt. Express **19**, 6829 (2011).

[23] L. Bergé, S. Skupin, F. Lederer, G. Méjean, J. Yu, J. Kasparian, E. Salmon, J. P. Wolf, M. Rodriguez, L. Wöste, R. Bourayou, and R. Sauerbrey, Phys. Rev. Lett. **92**, 225002 (2004).

[24] G. Méchain, C. D'Amico, Y.-B. André, S. Tzortzakis, M. Franco, B. Prade, A. Mysyrowicz, A. Couairon, E. Salmon, and R. Sauerbrey, Opt. Commun. **247**, 171 (2005).

[25] G. Méjean, J. Kasparian, J. Yu, E. Salmon, S. Frey, J.-P. Wolf, S. Skupin, A. Vinçotte, R. Nuter, S. Champeaux, and L. Bergé, Phys. Rev. E **72**, 026611 (2005).

[26] S. Henin, Y. Petit, J. Kasparian, J.-P. Wolf, A. Jochmann, S. D. Kraft, S. Bock, U. Schramm, R. Sauerbrey, W. M. Nakaema, K. Stelmaszczyk, P. Rohwetter, L. Wöste, C.-L. Soulez, S. Mauger, L. Bergé, and S. Skupin, Appl. Phys. B **100**, 77 (2010).

[27] D. Mongin, E. Schubert, N. Berti, J. Kasparian, and J.-P. Wolf, Phys. Rev. Lett. **118**, 133902 (2017).

[28] S. Eisenmann, J. Peñano, P. Sprangle, and A. Zigler, Phys. Rev. Lett. **100**, 155003 (2008).

[29] M. Petrarca, S. Henin, K. Stelmaszczyk, S. Bock, S. Kraft, U. Schramm, C. Vaneph, A. Vogel, J. Kasparian, R. Sauerbrey, K. Weber, L. Wöste, and J.-P. Wolf, Appl. Phys. Lett. **99**, 141103 (2011).

[30] G. Fibich, S. Eisenmann, B. Ilan, and A. Zigler, Opt. Lett. **29**, 1772 (2004).

[31] A. Dubietis, G. Tamošauskas, G. Fibich, and B. Ilan, Opt. Lett. **29**, 1126 (2004).

[32] C. Milián, V. Jukna, A. Couairon, A. Houard, B. Forestier, J. Carbonnel, Y. Liu, B. Prade, and A. Mysyrowicz, J. Phys. B: At., Mol. Opt. Phys. **48**, 094013 (2015).

[33] G. Méchain, A. Couairon, M. Franco, B. Prade, and A. Mysyrowicz, Phys. Rev. Lett. **93**, 035003 (2004).

[34] V. D. Zvorykin, I. V. Smetanin, N. N. Ustinovskii, and A. V. Shutov, Appl. Phys. B **124**, 80 (2018).

[35] F. Théberge, W. Liu, P. Tr. Simard, A. Becker, and S. L. Chin, Phys. Rev. E **74**, 036406 (2006).

[36] P. P. Kiran, S. Bagchi, S. R. Krishnan, C. L. Arnold, G. R. Kumar, and A. Couairon, Phys. Rev. A **82**, 013805 (2010).

[37] X.-L. Liu, X. Lu, X. Liu, T.-T. Xi, F. Liu, J.-L. Ma, and J. Zhang, Opt. Express **18**, 26007 (2010).

[38] Z. Q. Hao, R. Salamé, N. Lascoux, E. Salmon, P. Maioli, J. Kasparian, and J.-P. Wolf, Appl. Phys. B **94**, 243 (2009).

[39] O. G. Kosareva, W. Liu, N. A. Panov, J. Bernhardt, Z. Ji, M. Sharifi, R. Li, Z. Xu, J. Liu, Z. Wang, J. Ju, X. Lu, Y. Jiang, Y. Leng, X. Liang, V. P. Kandidov, and S. L. Chin, Laser Phys. **19**, 1776 (2009).

[40] G. Point, Y. Brelet, A. Houard, V. Jukna, C. Milián, J. Carbonnel, Y. Liu, A. Couairon, and A. Mysyrowicz, Phys. Rev. Lett. **112**, 223902 (2014).

[41] K. Lim, M. Durand, M. Baudelet, and M. Richardson, Sci. Rep. **4**, 7217 (2014).

[42] R. I. Grynko, D. L. Weerawarne, X. Gao, H. Liang, H. J. Meyer, K.-H. Hong, A. L. Gaeta, and B. Shim, Opt. Lett. **41**, 4064 (2016).

[43] S. Tzortzakis, M. A. Franco, Y. B. André, A. Chiron, B. Lamouroux, B. S. Prade, and A. Mysyrowicz, Phys. Rev. E **60**, R3505(R) (1999).

[44] S. Eisenmann, A. Pukhov, and A. Zigler, Phys. Rev. Lett. **98**, 155002 (2007).

[45] D. Abdollahpour, S. Suntsov, D. G. Papazoglou, and S. Tzortzakis, Opt. Express **19**, 16866 (2011).

[46] J. Yu, D. Mondelain, J. Kasparian, E. Salmon, S. Geffroy, C. Favre, V. Boutou, and J. P. Wolf, Appl. Opt. **42**, 7117 (2003).

[47] S. Tzortzakis, B. Prade, M. Franco, and A. Mysyrowicz, Opt. Commun. **181**, 123 (2000).

[48] C. Y. Chien, B. La Fontaine, A. Desparois, Z. Jiang, T. W. Johnston, J. C. Kieffer, H. Pépin, F. Vidal, and H. P. Mercure, Opt. Lett. **25**, 578 (2000).

[49] Y.-H. Chen, S. Varma, T. M. Antonsen, and H. M. Milchberg, Phys. Rev. Lett. **105**, 215005 (2010).

[50] X. Gao, G. Patwardhan, S. Schrauth, D. Zhu, T. Popmintchev, H. C. Kapteyn, M. M. Murnane, D. A. Romanov, R. J. Levis, and A. L. Gaeta, Phys. Rev. A **95**, 013412 (2017).

[51] G. Rodriguez, A. R. Valenzuela, B. Yellampalle, M. J. Schmitt, and K.-Y. Kim, J. Opt. Soc. Am. B **25**, 1988 (2008).

[52] T. D. Grow, A. A. Ishaaya, L. T. Vuong, A. L. Gaeta, N. Gavish, and G. Fibich, Opt. Express **14**, 5468 (2006).

[53] R. Benattar, C. Popovics, and R. Sigel, Rev. Sci. Instrum. **50**, 1583 (1979).

[54] N. L. Aleksandrov, S. B. Bodrov, M. V. Tsarev, A. A. Murzanev, Yu. A. Sergeev, Yu. A. Malkov, and A. N. Stepanov, Phys. Rev. E **94**, 013204 (2016).

[55] M. Takeda, H. Ina, and S. Kobayashi, J. Opt. Soc. Am. **72**, 156 (1982).